Microsystem Technologies (2026) 32:122
https://doi.org/10.1007/s00542-026-06070-9

TECHNICAL PAPER

Directly fixed and sealed ultra-thin membrane enables an autoclavable two-chamber bioreactor with selective permeability and optical access

Leona M. Speicher[1] · Khai Chau-Nguyen[1] · Laura Supp[1] · Ralf Ahrens[1] · Andreas E. Guber[1] · Jan G. Korvink[1] · Dario Mager[1]

Received: 5 November 2025 / Accepted: 7 April 2026

Abstract

An autoclavable microfluidic bioreactor (MBR) with an integrated gas-liquid contactor based on an ultra-thin permeable and transparent membrane enables a systematic analysis of intra-plant communication. The bioreactor units can be cascaded in a downstream manner, driven by a perfusion stream, to provide one-directional paths for allelochemical communication. Our article details a manufacturing pathway that achieves wrinkle-free membranes in these autoclaveable chips, by applying a drumhead-stretching design to the installed membrane. Traditional ultrasonic welding was used in the end as the bonding process, but absorber-free laser transmission welding was tested as well, and the results are reported in this article. In addition, we evaluated the membrane-stretching-behavior theoretically through simulations. The results of this analysis were then applied to the membrane installation. Through the new design and the application of the membrane stretching analysis, a reduction of the wrinkle amplitude in the installed membrane of on average over 80% was achieved, which in turn evened out the flow conditions in the MBRs. Therefore, in the future, the autoclavable bioreactors will be ready for cell culture experiments and the applied membrane integration provides an approach for other projects where ultra-thin permeable membranes need to be installed wrinkle-free.

1 Introduction

Often, plants that are stressed by abiotic stressors like extreme temperature, or drought, are more prone to attacks by their pathogens, such as grapevines attacked by fungi. The weakness typically manifests itself in poorer crop quality, a decrease in yield, and often in the underdevelopment of affected crops (Okoro et al. 2019; Elad and Pertot 2014). Therefore, the effect of climate change results not only in an ecological dimension, but also in a financial dimension.

The use of herbicides and fungicides, which exhibit general toxicity, has been the main approach of past decades to the treatment of encroaching pathogens. However, their use has a detrimental effect on the environment. Thus, novel and preferably sustainable approaches to plant protection have to be sought after, since climate change intensifies abiotic stresses on crops and plants in general. A promising approach targets plant-aggressor communication by identifying it and subsequently modifying or prohibiting it Metzger (2023); Khattab (2021); Okoro et al. (2019); Elad and Pertot (2014). The corresponding research can

✉ Dario Mager
dario.mager@kit.edu

Leona M. Speicher
leona.speicher@kit.edu

Khai Chau-Nguyen
khai.chau@kit.edu

Laura Supp
laura.supp@gmx.de

Ralf Ahrens
ralf.ahrens@kit.edu

Andreas E. Guber
andreas-guber@t-online.de

Jan G. Korvink
jan.korvink@kit.edu

[1] Karlsruhe Institute of Technology, Institute of Microstructure Technology, Hermann-von-Helmholtz-Platz 1, 73644 Eggenstein-Leopoldshafen, Baden-Württemberg, Germany

Published online: 10 July 2026

be conducted using the modular microfluidic bioreactor (MBR), presented in this paper, to dissect and monitor this plant-aggressor communication.

The MBR (Kreppenhofer 2013; Finkbeiner 2019; Schmidt-Speicher et al. 2021) is a modular microfluidic chip that allows the confined cultivation of plant cells and fungi separated from direct contact with each other, but with the potential to be interconnected via unidirectional fluidic pathways as shown in Fig. 1. The flow allows only downstream communication between the chambers, providing the researcher with a way to dissect and analyze how plant cells and their pathogens communicate with each other. Thus, individual interactions are singled out and can be evaluated in detail (Kreppenhofer 2013; Finkbeiner 2019; Schmidt-Speicher et al. 2021).

Several plant-on-chip systems, such as tobacco protoplast culture in polydimethylsiloxane (PDMS) microfluidic chips, have been developed over the years and were derived from generic lab-on-a-chip systems (Ko et al. 2006; Meier et al. 2010; Grossmann et al. 2011). However, PDMS-based systems are always prone to leaking and can not be autoclaved for sterilization. The MBR however is manufactured from the robust polymer polycarbonate (PC). Choosing PC renders the final plastic chips autoclavable (Metzger 2023; Inc 2024; AdvanTech 2021), but manufacturing methods are also more advanced compared to PDMS.

The concept is a systematically improved version of the microfluidic bioreactor from Kreppenhofer (2013), Finkbeiner (2019) and Finkbeiner et al. (2021). To achieve the smooth flow conditions required for successful plant cell cultivation and repeatability of experiments and also to prevent trapped air bubbles from sticking to edges or corners, an oval chamber shape was chosen (Finkbeiner 2019; Kreppenhofer 2013). The reactor has two sections: an upper cultivation chamber for the plant material and a lower supply chamber, perfused with nutrients and additives. The chambers are separated by a $19\mu\mathrm{m}$ thick permeable membrane, with a pore size of $5\mu\mathrm{m}$ and made of polyester (PETE, membrane no.: 130008) by Sterlitech (Auburn, WA, USA). The membrane prevents the plant cells from being flushed out of the cultivation chamber while at the same time allowing nutrients from the supply flow to diffuse into the chamber. In addition, metabolomic compounds from plant cells are allowed to flow out of the cultivation chamber through the membrane to the supply chamber and on, into the communication channel. The membrane thus implements a definable permeability that can be easily adapted through selection of the desired pore size. Figure 2 provides a top and side view of the MBR.

The MBR chip halves are hot-embossed from PC raw stock. Using this process, MBRs can be manufactured rapidly and economically. Together with a practicable size of the MBR $(2.5\,\mathrm{cm} \times 7.5\,\mathrm{cm})$, to match the size of a standard glass slide, the microfluidic system is well adapted for microscopy, as shown from the cultivation results in Fig. 3.

Versions of the MBR have been successfully autoclaved for and applied in several experiments over the years. The initial designs were used, for example, by Finkbeiner (2019) to cultivate BY2 cells, two cell lines of *Catharantus roseus*, and *Taxus chinesis*. In Finkbeiner et al. (2021) these applications experiments were further expanded by first cultivation experiments with *Neofusicoccum parvum* (*N. parvum*) in the MBR. A BY2 culture in a downstream MBR was added to the *N. parvum* setup, creating the first inter-kingdom communication experiment.

Because flow conditions are so delicate and vital to successful cell cultivation and experiments, they were assessed in detail. First, Finkbeiner (2019) evaluated whether the applied membrane allowed enough nutrients to diffuse through to the cultivation chamber using a simulation and validation approach. The results showed that sufficient

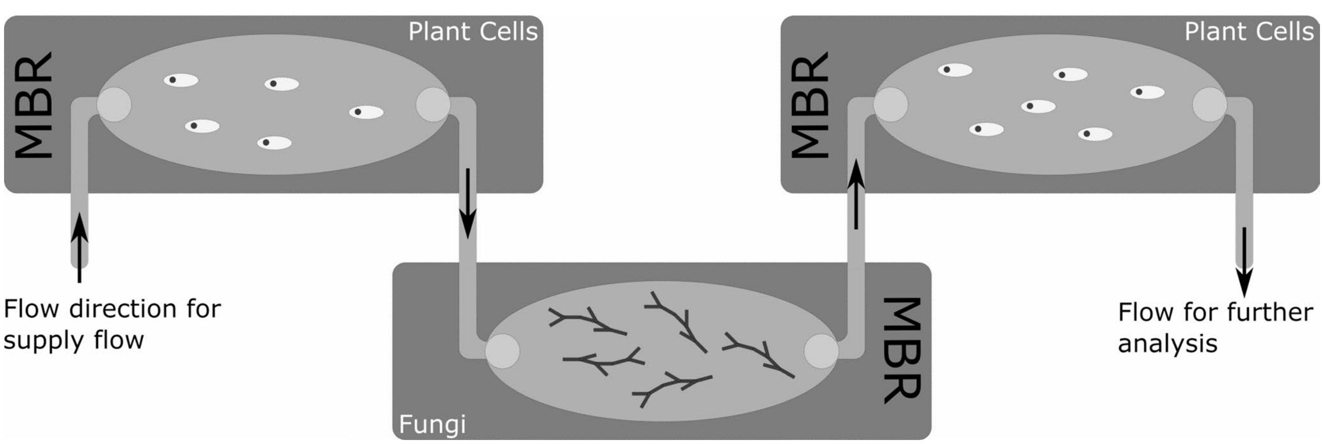

Fig. 1 Principle of microfluidic bioreactors connected through unidirectional flow channels. Chemical communication is limited to the downstream direction through uni-directional perfusion.

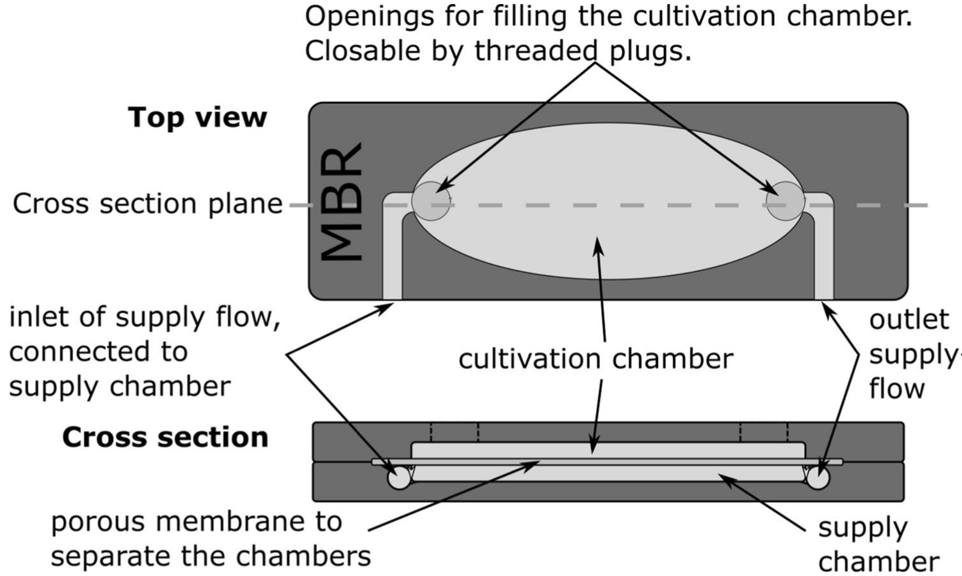

Fig. 2 The microfluidic bioreactor for plant cell cultivation consists of an upper chamber for plant cell cultivation and optical examination, and a lower supply chamber connected to other fluidic network elements. The two chambers are separated by a membrane with predefined permeability.

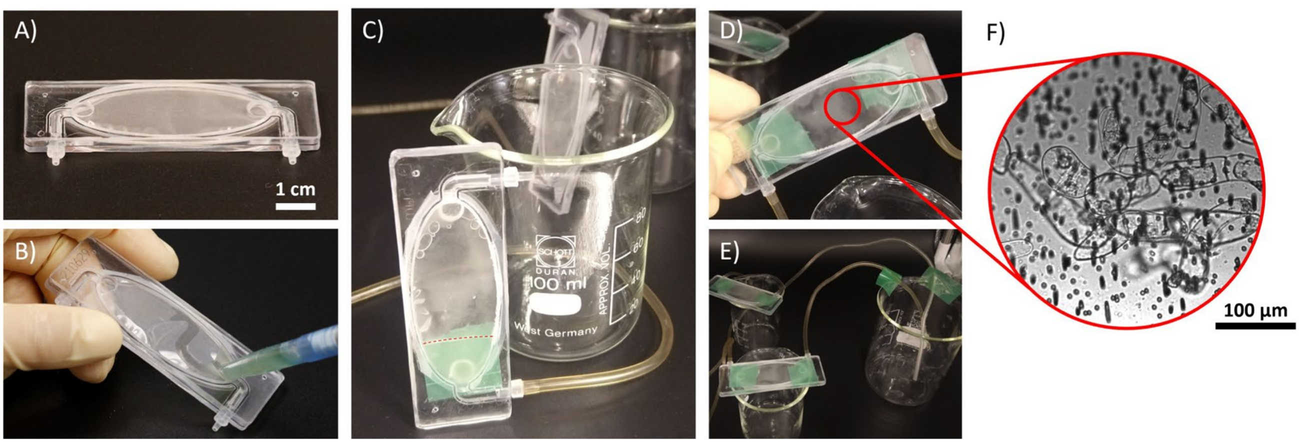

Fig. 3 Microfluidic bioreactor in use. A) A microfluidic bioreactor before filling. B) The plant cell cultivation is filled slowly from one side into the MBR using an Eppendorf pipette that has been cut to fit the opening of the cultivation chamber. C) The MBR is filled with the nutrient solution standing upright to eliminate from the cell-filling remaining air bubbles. D) shows a microfluidic bioreactor filled with a suspension of BY2 plant cells. The cloudiness is caused by the plant cell suspension filled into the MBR. E) Setup for the cultivation of plant cells in the MBR. The individual reactors are hooked up via tubes to syringe pumps that diffuse the MBRs with a nutrient solution during the cultivation period F)The round picture shows the BY2 plant cells using a microscope. The plant cells are visible as the outlined but see-through structures in the front. The porous membrane is visible in the background.

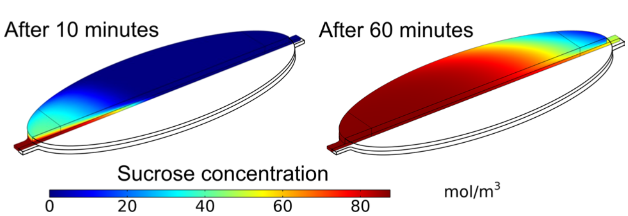

Fig. 4 3D-simulation of nutrient distribution throughout the cultivation chamber. Since, the chamber is symmetrical, only half of it was simulated.

maltose and sucrose can diffuse through the membrane to cater to the nutrition of cultivated plant cells.

Schmidt-Speicher et al. (2021) examined in 2D- and 3D-simulations if the flow conditions allowed nutrients to be evenly distributed and how long it takes to supply nutrients all the way to the boundaries of the cultivation chamber. The cultivation chamber has a volume of 800 μL, and if the targeted flow rate of 20 μL/min was applied to simply fill this volume without considering any kind of geometric or perfusion effects, it would take 40 min. The simulations conducted considered such effects, and the 3D simulations showed that it takes about 60 min to distribute nutrients throughout 67% of the chamber (as shown in Fig. 4) and approximately 160 min to reach the maximal expected concentration of nutrients throughout the entire volume.

Since typical plant cell experiments run for several hours to several days (Metzger 2023; Khattab 2021; Kreppenhofer

2013; Finkbeiner 2019), this filling process is reasonably fast.

However, when the flow conditions were compared to reality, the flow differed significantly from the simulated tests. This is most likely, because previous design processes focused on getting a prototype running, while at this point of the development of the MBR a more precise analysis of and approach to the manufacturing of the setup was taken.

If no membrane was installed prior to closing the MBR, the flow tests matched the simulated behavior well (see Fig. 5C). Thus, the general layout of the MBR worked as intended. Once the membrane was further analyzed, it was identified that during the installation process, the membrane wrinkled. In Fig. 5A) an MBR is depicted that was manufactured and closed using the current design and the ultrasonic welding process. The wrinkles can be seen here very well. Figure 5B) shows the resulting flow pattern if a membrane is installed and Fig. 5C) the resulting flow if the MBR is assembled without any barrier between the cultivation and the supply chamber, so the ideal flow conditions throughout the MBR.

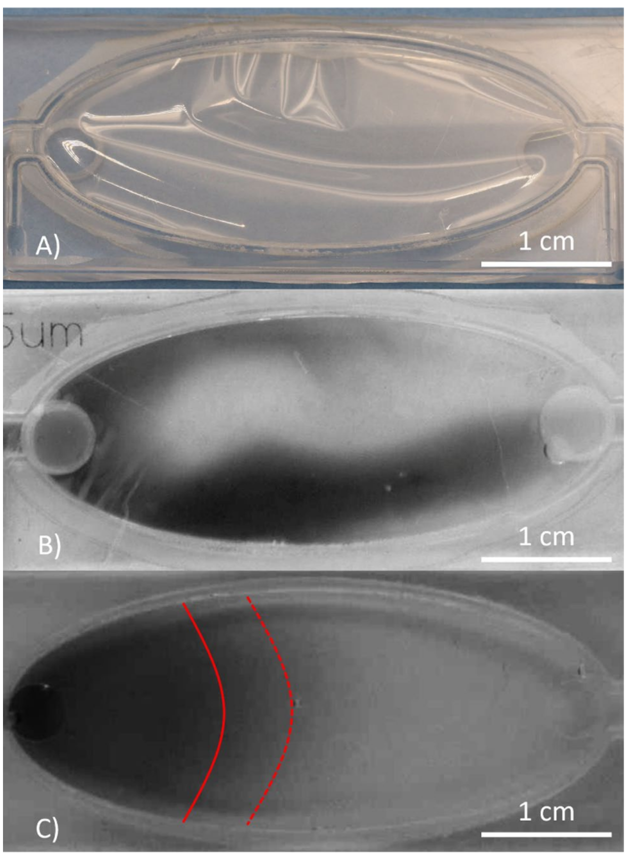

Fig. 5 Testing flow profiles developing in an MBR (Application of colored water as a stand-in for the nutrient solution applied in plant cell cultivations. Recording with a monochrome camera (uEye SE (UI-2220SE-M-BG) by IDS Imaging Development Systems GmbH, Obersulm, Germany)). **A)** An MBR welded shut with a continuous ED using USW. The membrane develops strong wrinkles due to the ultrasonic movement during the welding process. **B)** The resulting flow profile. In the present state, the wrinkles deter the profile from optimal conditions. **C)** Flow profile of an MBR which is closed without a membrane separating the two chambers. This time, the occurring flow profile matches the simulations well.

Experiments were conducted to determine whether warping of the membrane created a significant issue. For this, suspensions of BY2 plant cells were transferred to 17 MBRs. Although in some cases the cells could be inserted into the cultivation chamber and distributed there evenly, in more than half the cases wrinkles prevented the cells from spreading evenly throughout the cultivation chamber, which could be clearly observed visually, or cells could not be inserted at all. Furthermore, when investigating how a pH-changing trigger compound affected the metabolism of cells, subsequent pH measurements at the outlet of the cultivation chamber showed no repeatability but rather local peaks depending on the amount of cells available to process the trigger compound. This confirmed that the wrinkled installation of the membrane caused a significant disturbance of the flow and thus the cultivation conditions and needed to be fixed (Metzger 2023).

Following these results, the installation of membranes and thin foils was investigated in detail based on the existing literature. After a brief clarification regarding the terminology of thin and ultra-thin foils, the findings from the literature are summarized.

In literature, thin foils typically have thicknesses of several hundred micrometers (Espinoza Orías and Renaud 2004; Tsiangou et al. 2020; Dobrota and Lazar 2021; Korycki et al. 2023; Brosda et al. 2020). Foils are termed“ultra-thin”when their thickness ranges from several hundred nanometers to 100 μm (Shah 2012; Tang et al. 2020; Li et al. 2021), although these limits depend on the material. In this work,“membrane”is used as a subcategory of “foil”following Focke et al. (2010); Jong et al. (2006), referring to an ultra-thin, functionalized foil with selected permeability.

Several studies describe the installation of thin foils made from various materials, such as palladium for the generation of H_2Boeltken et al. (2014), cellulose for filtration (Tang et al. 2020), and carbon paper for proton exchange membranes in fuel cells Dang et al. (2019). However, the installation of polymer foils and membranes is less well covered despite their widespread use in food and medical packaging, microfluidic fabrication, and thermoset composite production for lightweight structures.

The most straightforward method for bonding two thermoplastic polymers without additives is to heat them above their glass transition temperature, press them together to tangle the individual polymer chains, and cool the joint below the transition temperature to stabilize the bond. This heat or hot plate welding process has been a standard in the polymer industry for more than six decades (Focke et al. 2010; Qiu et al. 2020; Iwasiro et al. 2014; Scheffler and Leao 2008; Wood and Blasko 204). It remains widely used due to its reliability and the high bond strength it achieves compared to ultrasonic welding (Wood and Blasko 204; Plastic Welding and Solutions 2024). However, several studies report difficulties in applying this method to thin foils. For example, strong geometric distortions and uncontrolled wrinkling occurred in polypropylene air-mattress elements due to significant thermal expansion and contraction (Scheffler and Leao 2008). Similarly, polycarbonate, polyethylene terephthalate (PET), and polyimide membranes spanning a chamber sagged and bonded unintentionally to the chamber floor when heated during installation (Kreppenhofer 2013).

Ultrasonic welding focuses the introduced energy more precisely and confines heat generation to a small area. It is a well-established process for thermoplastics based on frictional heating through high-frequency vibrations between the joining partners (Potente 2004; Rotheiser 2009). Common applications include food and medical packaging (Focke et al. 2010). Reported issues include damage to sensitive electronics from vibrations (Dahlstrand 2017), membrane tearing (Schmidt-Speicher et al. 2021), and visible wrinkle formation in bonded foils (Dobrota and Lazar 2021; Speicher et al. 2023). Few studies explicitly discuss the challenges of wrinkling, referred to as 'diaphragming' or 'oil canning effect', caused by vibrations in foils welded over large openings, as observed in the MBR. Only one source, a manufacturer, suggested mitigating these problems through reducing the vibration amplitude by either dampening the weld zone or using higher operating frequencies, although the latter requires costly new equipment (Dukane Intelligent Assembly 2024).

The third process, laser transmission welding, is the most versatile. Like ultrasonic welding, it allows localized energy input, but its optical beam guidance allows for any 2D contour conforming to the part geometry, making it more agile than the other two methods (Brosda et al. 2020; Potente 2004; Beck et al. 2002; Brosda et al. 2020). Typically, an absorbing layer is required, either as part of the lower substrate (Pagano et al. 2017) or as an added dye (Klotzbuecher et al. 2006; Beck et al. 2002; Jiang et al. 2015; Liu et al. 2017). Reported challenges include ensuring proper clamping to maintain alignment and avoid air entrapment – which can lead to incineration (Beck et al. 2002; Brown et al. 2000) – and preventing material degradation from intense localized heating common in thermoplastics with narrow processing windows (Pagano et al. 2017). Even without degradation, polymers may sag or distort due to rapid temperature changes (Beck et al. 2002; Brown et al. 2000; Jiang et al. 2015). High weld quality requires precise process control to prevent bubble formation (Brown et al. 2000; Liu et al. 2017), off-center heat-affected zones (Brosda et al. 2020), or degradation at the weld centerline (Pagano et al. 2017). However, there is little literature on welding polycarbonate without absorbing dyes or layers, and none was found on absorber-free welding of thin PET foils to bulk substrates in quasi-simultaneous or contour-welding modes.

2 Results

2.1 Simulated membranes

To evaluate the membrane stretch, two geometries were studied as introduced in Sec. 3.1. Further analysis was necessary due to the creation of wrinkles during the ultrasonic bonding process (cf. Sec. 1) which created wrinkles with an amplitude of several hundred micrometers up to $0.75\,\mathrm{mm}$ Speicher et al. (2023).

The oval shape elucidates the behavior of the membrane in the MBR. The round shape causes an even distribution of the stress load throughout the entire membrane. It can be seen in Figs. 6A and B the simulation shows that an even line load around the perimeter leads to a homogeneous von Mises stress distribution throughout the entire membrane where every area is equally strained. The corresponding displacement simulation in Fig. 6C shows that this leads to a circular displacement profile with no displacement in the center of the circular membrane and a higher displacement the further out of the center it gets. Figure 6F shows the von Mises stress simulated throughout the oval-shaped membrane. An even line load following the oval shape is applied as visualized in Fig. 6E and the simulation displays lower stress loads in the center area of the oval-shaped membrane and higher loads in the flat ends of the oval which fade toward the narrow ends of the oval. The according displacement simulation is displayed in Fig. 6H and shows a displacement that results in no stretching in the center area of the oval and the highest stretch of the material at the narrow ends of the oval.

2.2 Pillar-and-groove-design for ultrasonic welding of MBR

In Sec. 3.2 the pillar-and-groove-joint is introduced in general. Since a satisfactory manufacturing result could not be achieved using a continuous energy director (ED), a pillar-and-groove joint for the MBR was designed. This reduces the risk of imperfect weld seams, which occur repeatedly when long continuous weld seams – like in the previous design – are implemented because the process for these lengths has more variable parameters that each have to be controlled exactly. Shorter welded areas that furthermore

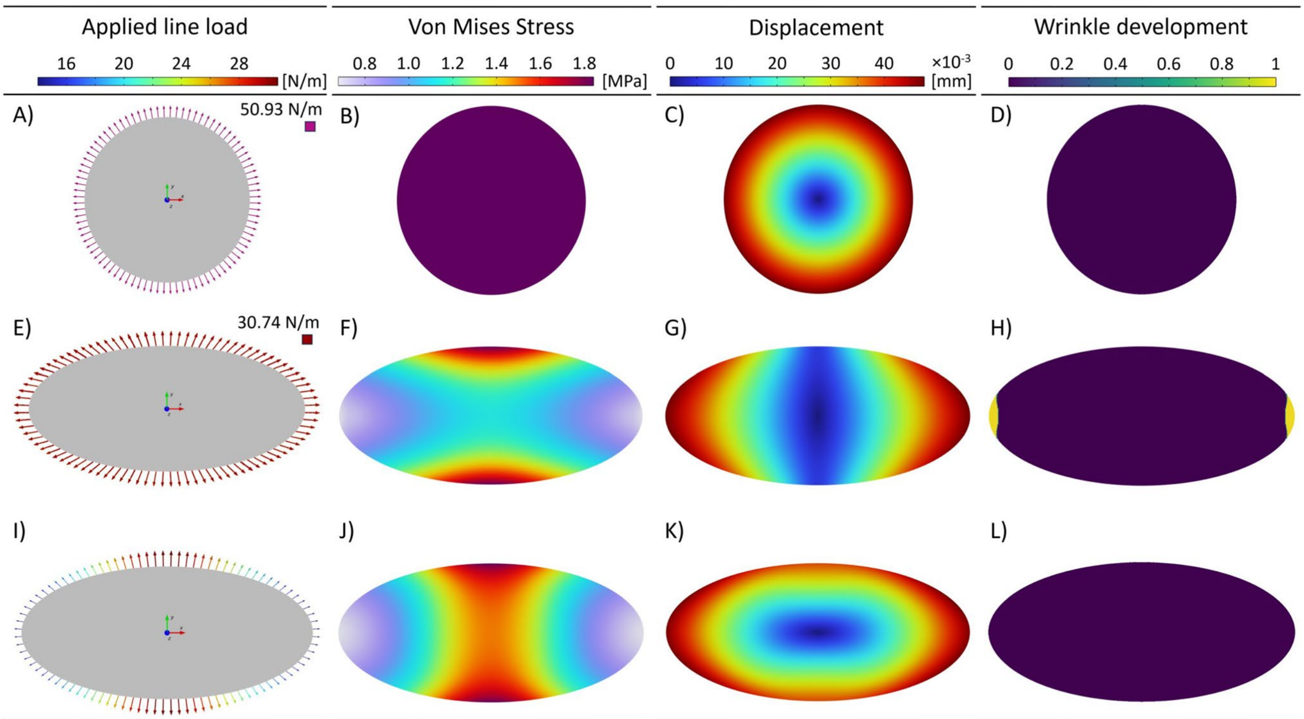

Fig. 6 Setup and results of the stress and stretch simulation. **A)**, **E)**, **I)** display the applied line loads, **B)**, **F)**, **J)** show the resulting von Mises Stress, **C)**, **G)**, **K)** depict the membrane stretching behavior caused by the stress profile, and **D)**, **H)**, **L)** visualize possible hot spots of wrinkle appearance in the membrane. As can be spotted well from part B) a round line load on a circular-shaped membrane results in an even stress distribution which in turn leads to an even displacement of the membrane. The current geometry and line load distribution are displayed in row 2, where Fig. **F**) clearly shows the uneven stress conditions that result in an uneven displacement profile. Row 3 shows a possible optimization where the original oval chamber geometry is kept, because it has been shown to be the ideal shape for the chamber, but applying a circular line load to it. This could be realized by, e.g., placing the pins spanning the membrane on a circular perimeter. The resulting displacement profile (**K**) is more evened out and comparable to the circular-shaped chamber – ideal for even displacement – shown in **C)**.

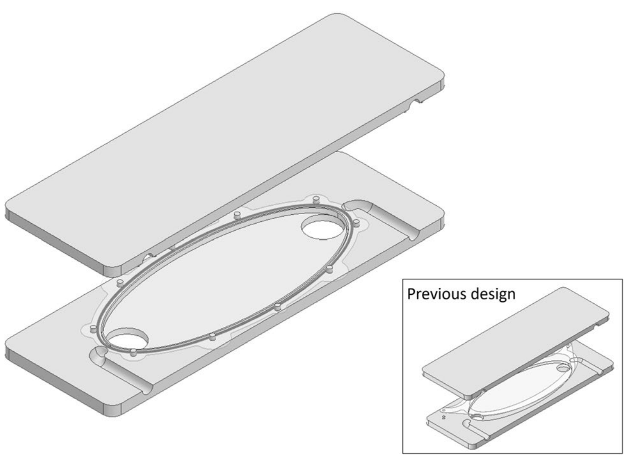

Fig. 7 Revised design for welding the microfluidic bioreactor ultrasonically. The ultra-thin membrane is not welded and thus melted directly. Instead, it is secured with ten pins evenly distributed around the perimeter and stretched across a $0.5\,\mathrm{mm}$ sealing ring during the weld. This way, a leak-proof seal can be achieved while fixing the membrane as a barrier between the chambers without breaking its structural integrity.

sit in specified grooves, as is the case for the pillar-and-groove joints, have fewer variables and, through the groove, additional guidance during the weld. As can be seen from Fig. 7 – which displays this revised design – the membrane is therefore not welded along the perimeter of the chamber, but instead stretched across a sealing ring (diameter of $0.5\,\mathrm{mm}$) which spans and tightens it. At the same time, this sealing ring enables leak-free sealing of the chambers when pressed during the welding process.

The corresponding weld parameters can be seen in Table 1. The weld was performed using an energy-controlled process with a limiting energy introduction of $82\,\mathrm{J}$. The collapse distance during the weld was $0.33\,\mathrm{mm}$, leading to a $0.207\,\mathrm{mm}$ compression of the sealing-ring. The applied sealing-ring has a cross-section of $0.5\,\mathrm{mm}$ and spans a diameter of $38\,\mathrm{mm}$. It is made from fluorocarbon-based fluoroelastomer (FKM) by the Industrie Dichtungs Service (IDS, Willich, Germany), has a hardness of 75°Shore and is FDA-conform. The compression deformation was tested prior to installing the seal rings and the results can be found in the App. B.

Table 1 Ultrasonic welding parameters used for the adapted design of the MBR. The new design uses ten pillar-and-groove joints spaced evenly around the perimeter of the chambers.

Welding parameters	Value
Membrane thickness [μm]	19
Welding mode	Energy controlled
Introduced welding energy [J]	113
Total Welding collapse [mm]	0.34
Welding force [N]	400
Holding period [s]	1
Amplitude [μm]	24.38

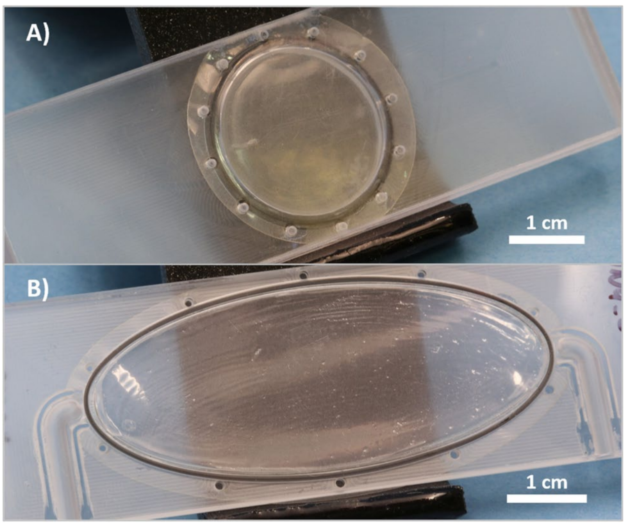

Fig. 8 **A)** A round membrane stretched across a sealing ring with a cord size of 1 mm and a diameter of 20 mm. This way, the created setup still fits within the area of a standard glass slide (25 mm x 75 mm) and complies with the size of the microfluidic bioreactor. As can be easily seen in the photograph, the membrane shows almost no wrinkles. **B)** A welded MBR of the new ultrasonic design, applying the drumhead-stretching approach when installing the membrane. The ten pins pulling the membrane out as well as the black sealing ring across which the membrane is spanned can be spotted well in the picture. The MBR propped up to increase the visibility of any wrinkles in the membrane. There are a few wrinkles that are aligned along the long axis of the oval that can be seen well. These are in accordance with the simulated stress load and displacement. They are caused by the uneven stress and originate in imperfections, most likely created by the milling while manufacturing the chip halves.

2.3 Comparison of simulated membrane behavior and manufactured chips

Figure 8A shows a round membrane stretched over a sealing ring like a drumhead. This setup is similar to the round membrane evaluated with a circular line load through the simulation. It should be noted that, instead of a constant circular line load, the membrane is spanned by ten ten-pins evenly spaced around the perimeter. Furthermore, imperfections are always present in manufactured parts, which cause modifications of the stretching behavior deviating form the simulation results created with ideal boundary conditions.

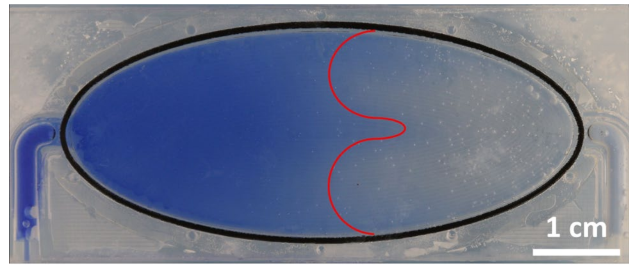

Fig. 9 Visualising of the flow conditions in the MBR. The MBR was initially filled with deionized water and then blue dyed water was applied through the inlet pushed by a syringe pump at $20\,\mu\mathrm{Lmin}^{-1}$. The pictures show the filling status after 70 min. The flow profile is not as perfect as is shown in Fig. 5C) when no membrane is installed between the two chambers. Instead, the flow profile develops a spike in the centre of the MBR, but the flow follows this spike evenly on both sides throughout the entire filling process, thus, creating a significantly more even growth condition than in Fig. 5B).

Thus, minor wrinkles are expected from this initially uneven stress condition. However, these wrinkles are comparatively small and the displacement profile is quite even. Thus, this setup is comparable to the simulation results of a round-shaped membrane presented in Fig. 6A to D.

The welded MBR of this version is depicted in Fig. 8B. To capture the light reflections so that any wrinkles in the membrane can be spotted well, the MBR is propped up. As can be seen, the membrane installation was not completely wrinkle-free. Wrinkles with an on average amplitude of 125 μm remained present. This is due to the uneven stress load distribution, which was evaluated theoretically in Sec. 3.1 and the results presented in Sec. 2.1. In addition, the milling process is a good and precise manufacturing process, but minor imperfections in the milled parts are to be expected. Furthermore, the ideal boundary conditions assumed for the theoretical analysis should be kept in mind. Thus, minor wrinkle formation is to be expected in manufactured parts, as these imperfections can serve as a point of origin for wrinkle formation due to uneven stress load distribution throughout the oval-shaped membrane. These imperfections can also lead to the curving of wrinkles. For the future, a fast replication process for the chip halves such as hot embossing or injection molding would be favorable. These processes use molds for the part-replication that are usually created with higher precision, as any imperfection of the mold will be replicated in every cast part. However, at this point an amplitude reduction of over 80% was already achieved.

2.4 Validation of theoretical flow conditions

Figure 9 shows the flow conditions in the adapted design for ultrasonic welding introduced in Sec. 3.2. The filling status is depicted after a run-time of 70 min. The red line helps to see the flow profile developed, which is even on the sides of the filled chamber but shows a spike in the center as well. This spike prevailed throughout the filling process, but the sides also followed it evenly throughout the entire process runtime. Thus, it can be concluded that while the ideal flow conditions presented in Sec. 1 are not met, the flow profile has evened out significantly compared to the faulty flow profile before optimization (see Fig. 5). Furthermore, the flow is now symmetrical, and so are the wrinkles along the long axis of the oval-shaped chambers, which most likely result from the pins spanning the membrane being placed on an oval path. A preliminary visual assessment of the revised flow profile, together with an initial filling experiment of a single MBR conducted by a collaborating biologist, led to provisional design approval from their side. Further systematic testing and detailed evaluation will be conducted in the next years to thoroughly assess the new design's suitability for biological experiments.

As reviewed in Sec. 2.1 an oval line load leads to an inhomogeneous displacement profile throughout the membrane, despite the stress distribution following the oval geometry smoothly. If a circular line load was applied to the otherwise oval shape, the displacement profile would even out as shown in Fig. 6I to L. Thus, a circular placement of the pins that stretch the membrane would be expected to create fewer wrinkles throughout the membrane.

2.5 Further simulations for optimizing cultivation conditions in the MBR

There are several approaches to further even out the cultivation conditions in the MBR and thus improve them. Regarding the topic of this article, two main areas were further examined: 1) improving the installation of the membrane and, 2) refining the way nutrient flow is provided through the supply chamber to the cultivation chamber in order to distribute nutrients faster or more equally. For a faster analysis, these evaluations were only done in 2D.

Concerning the improvement of membrane installation, a simulation was done to check if a circular line load on the oval-shaped chamber geometry would even the displacement and stress distribution. Figure 6I to L show this approach. In depiction (I), the circular line load is displayed. The image shows that the closer the load gets to the narrow edges at the ends of the oval, the less relative load is imposed on the membrane. The graphic (J) shows the simulation results of the resulting von Mises stress when a circular line load is applied. There is an area of higher stress load in the center area which gradually decreases as it gets closer to the narrow edges of the oval, thus coinciding obviously with the line load. Finally, picture (K) displays the simulation results of the material displacement arising from this load condition, and graphic (L) the simulation wrinkle development. As in the simulation of the round line load imposed on the circular-shaped membrane shown in Fig. 6A to D, an even displacement throughout the oval-shaped geometry is found.

The behavior of the simulated membrane shows a very even distribution of stress and displacement. Of course, this has to be analyzed with caution, as the simulation depicts a perfect situation. In the manufactured parts, minor imperfections would always be present and would serve as the point of origin for inhomogeneous displacement or stress distributions. The circular displacement and stress distribution correspond well to the expected results for the application of a circular load. In addition, because of the similar circular line load, the displacement of the oval-shaped area results in a centroid-related displacement profile comparable to its round counterpart and ideal for avoiding wrinkle generation when welding such a membrane. Subsequently, the incoherence between line load and area shape leads to an uneven stress distribution with lower strain in areas of lower imposed loads, as is the case in the narrow ends of the oval.

Since a round membrane with a circular line load showed a promising stretching behavior (cf. Figure 6 and Fig. 8A) we checked if a change of the chamber geometry from oval to round would be feasible with respect to the even and timely distribution of nutrients. To do so, a simulation comparable to the one in Fig. 4 was set up. The volume and height of the chamber geometry were kept the same and thus the radius of the circular geometry was set to $15.96\,\mathrm{mm}$. Due to this strong increase in the radius, the flow velocity in the chamber decreases twelve times compared to the flow velocity at the inlet. The overall flow profile is inhomogeneous, as can be seen well from the simulation visualization in Fig. 10. The analysis shows that it takes $40\,\mathrm{min}$ to achieve at least half the desired nutrient concentration in the whole round chamber, making it 61% slower than for the original oval shape.

To improve flow conditions so that nutrients are distributed faster and more evenly throughout the chamber, several approaches were evaluated. Some selected ones are presented here. An approach was to change the inlet channel to contact the supply chamber from underneath in the center (see Fig. 11A). In this way, the highest concentration of nutrients was placed in the center of the MBR and could flow evenly outward toward the narrow ends of the oval-shaped chambers. The simulation results showed that after only $47\,\mathrm{min}$, the desired concentration of nutrients could be expected throughout the entire chamber.

Furthermore, a change in the geometry of the supply chamber was analyzed to determine whether the distribution of nutrients to the cultivation chamber could be even out. Two approaches for this scenario are also presented

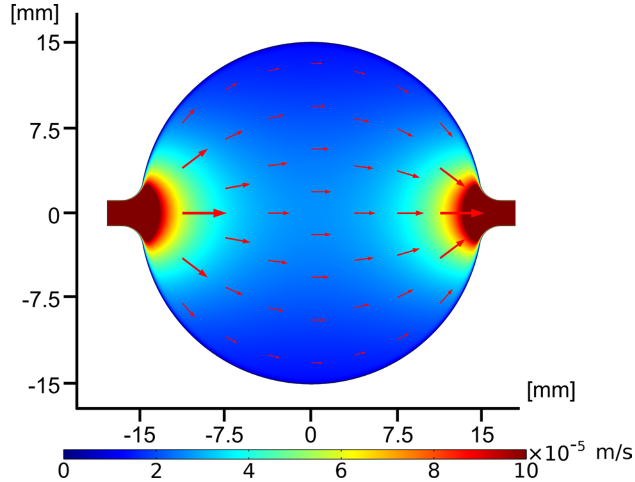

Fig. 10 Simulation of the nutrient distribution throughout a round-shaped chamber. The size of the red arrows corresponds to the relative flow velocity at the according point, while the direction of the arrow indicates the flow direction. The legend below assigns field plot colors to the velocity magnitude.

in Fig. 11: (B) shows a supply chamber with several pillars inserted throughout the area. These pillars help divide the nutrients supplied and distribute them more quickly to the outer areas. It takes about 23 min in order to reach at least half the desired concentration throughout the entire chamber.

A second approach was to divide the supply chamber into three channels (Fig. 11C). The simulation results show that a quick and initially even more homogeneous distribution of nutrients can be achieved. For this design, it takes only 32 min to achieve the desired concentration of nutrients in all areas.

In general, these three changes to the flow profile in the supply chamber all accelerated the expected nutrient supply throughout the cultivation chamber. However, for designs B) and C) the white areas represent walls and pillars that would have to be added to the supply chamber. Although this speeds up the even distribution of nutrients in the flooded area, the spots in the cultivation chamber above these wall areas (colored white) might receive fewer nutrients or these spots might reach the target nutrient concentration significantly later than the directly connected spots. In addition,

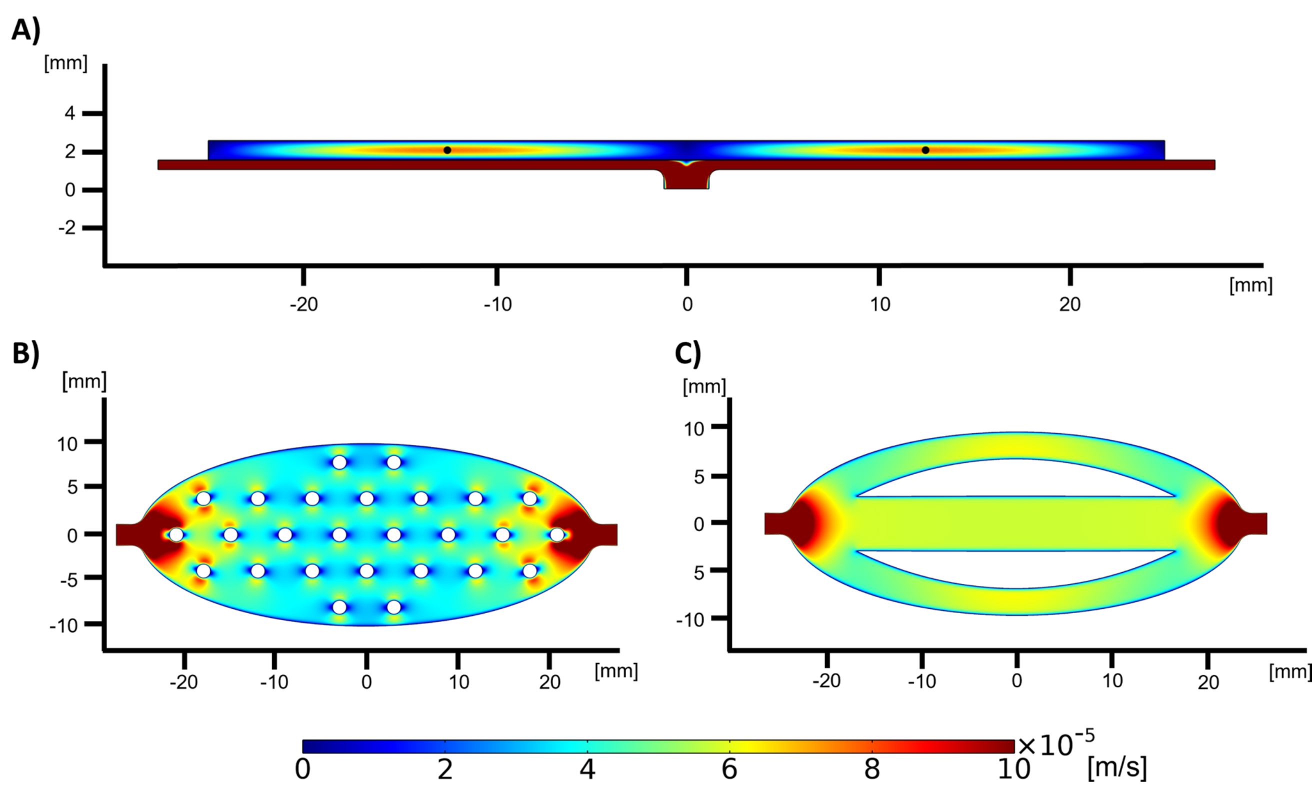

Fig. 11 2D-Optimisation approaches, improving the nutrient distribution throughout the supply chamber of the MBR. **A)** presents the simulation results if the supply chamber was contacted from underneath instead of from one side. This could decrease the time which is needed to achieve a high nutrient concentration in a large center area, which is also the area most likely analyzed at first under a microscope. **B)** depicts an MBR where several pillars are inserted into the supply chamber and how this would affect the nutrient distribution throughout it. It is derived from a split-and-recombine mixer common in microfluidics. Finally, **C)** shows the nutrient distribution if the chamber would be split up into three separate channels. This setup was analyzed due to its potential to help with membrane sagging. In all three plots, the position-dependent nutrient concentration is plotted as a scalar field value according to the legend below.

all three of them would come with major geometry changes, making the remanufacturing of the replication molds necessary. In the case of contacting the supply chamber from underneath in the center, the replication process would have to be changed, since such complex 3D-structures cannot be replicated using hot embossing with reasonable effort.

The chip halves for the second and third approach – where obstacles are placed in the supply chamber – can be replicated using the current process (hot embossing). But the pillars necessary for the approach in Fig. 11B require special attention when being hot embossed, because structures with a high aspect ratio (correlating the height of a structure to its cross section) are generally difficult to remove from their mold. Furthermore, a difficult assembly process is expected because the membrane would have to be attached to each of the individual pillars to ensure proper installation.

The third approach evaluated with the three channels instead of a completely open supply chamber is easier to replicate with the hot embossing process compared to the previous two options. However, the installation of the membrane between the supply and the cultivation chamber would be more difficult, similar to the pillar approach. For these reasons, so far none of these optimizations have been manufactured and tested, but the simulations were suitable ways to explore further options.

3 Methods

3.1 Simulating membrane stretch

A theoretical analysis of the membrane behavior during the manufacturing process gives more insight into suitable manufacturing approaches. For this, we assumed that the behavior of the membrane is symmetric with respect to two planes crossing the semi-major and semi-minor axes. For this reason, the computational model of the membrane can be simplified by adding essential constraints. The simulation is executed in a quarter model by adding two symmetric Dirichlet boundary conditions on the corresponding symmetry planes $\mathrm{u} \cdot \mathrm{n} = 0$, where n denotes the normal vector of the symmetry plane. Assume that the coordinate system is placed at the centroid of the membrane, its geometry can generally be described as an ellipse $x^2/a^2 + y^2/b^2 = 1$. In addition to the ellipsoid geometry, a circular geometry was also evaluated, where $a = b = 1$ was applied. In each case, a distributed line load is applied on the external boundary with two load cases $\mathbf{F_1} = \mathrm{F}_0[\ 1/a \quad 1/b \quad 0\ ]^T \cdot \mathbf{n_\Gamma}$ and $\mathbf{F_2} = \mathrm{F}_0[\ 1 \quad 1 \quad 0\ ]^T \cdot \mathbf{n_\Gamma}$ as given in Sec. 2.1 (Fig. 6).

In modified membrane theory, the properties of wrinkles are introduced on the mean surface of the membrane. Two techniques can be employed to extend conventional membrane theory by incorporating tension field theory. One involves presenting the relaxed strain energy density, while the other involves adjusting the deformation gradient. The former is limited to isotropic membranes, whereas the latter offers a wider applicability across different membrane types (Roddeman et al. 1987). The initial configuration of the membrane is described using material coordinates X, Y, and Z. The direction of uniaxial stress lies along the X-axis, Y denotes the direction of wrinkling, and Z represents the normal plane to the membrane as given in Fig. 12. The deformed configuration is denoted in lower-case symbols by coordinates x, y, and z. The membrane can be in one of the following three states after deformation:

- A taut state is observed when both in-plane principal stresses are positive and no improved deformation tensor is required.
- A wrinkled state occurs if one of the principal stresses is negative, requiring a modification of the deformation gradient tensor.
- A slack state arises when both principal stresses are negative, causing the neglection of the stress tensor.

As shown in Fig. 12, the mapping scheme is executed from the reference configuration to a fictitious lengthened one, ensuring that the current area matches the actual wrinkled zone. Assuming that uniaxial extension occurs in the $\mathbf{n_1}$ direction and $\mathbf{n_2}$ is the wrinkling direction, the modified deformation tensor $\bar{\mathrm{F}}$ is defined as

$$\bar{\mathrm{F}} = (\mathrm{I} + \beta \mathbf{n_2} \otimes \mathbf{n_2}) \cdot \mathrm{F}, \tag{1}$$

where I is the unity tensor and β is the wrinkling parameter ($\beta = 0$ in the taut state). According to the orthogonality condition in tension field theory:

$$\begin{aligned} \mathbf{n_1} \cdot \sigma \cdot \mathbf{n_2} &= 0, \\ \mathbf{n_2} \cdot \sigma \cdot \mathbf{n_2} &= 0, \end{aligned} \tag{2}$$

where σ is the Cauchy stress tensor derived from the second Piola-Kirchhoff stress tensor S,

$$\sigma = J^{-1} \bar{\mathrm{F}} \cdot \mathrm{S}(\bar{\mathrm{F}}) \cdot \bar{\mathrm{F}}^T, \tag{3}$$

with

$$J = \det(\bar{\mathrm{F}}^T). \tag{4}$$

The wrinkling condition is determined as follows

$$\mathbf{n_2} \cdot J^{-1} \bar{\mathrm{F}} \cdot \mathrm{S}(\bar{\mathrm{F}}) \cdot \bar{\mathrm{F}}^T = 0. \tag{5}$$

Fig. 12 Kinematics of wrinkling.

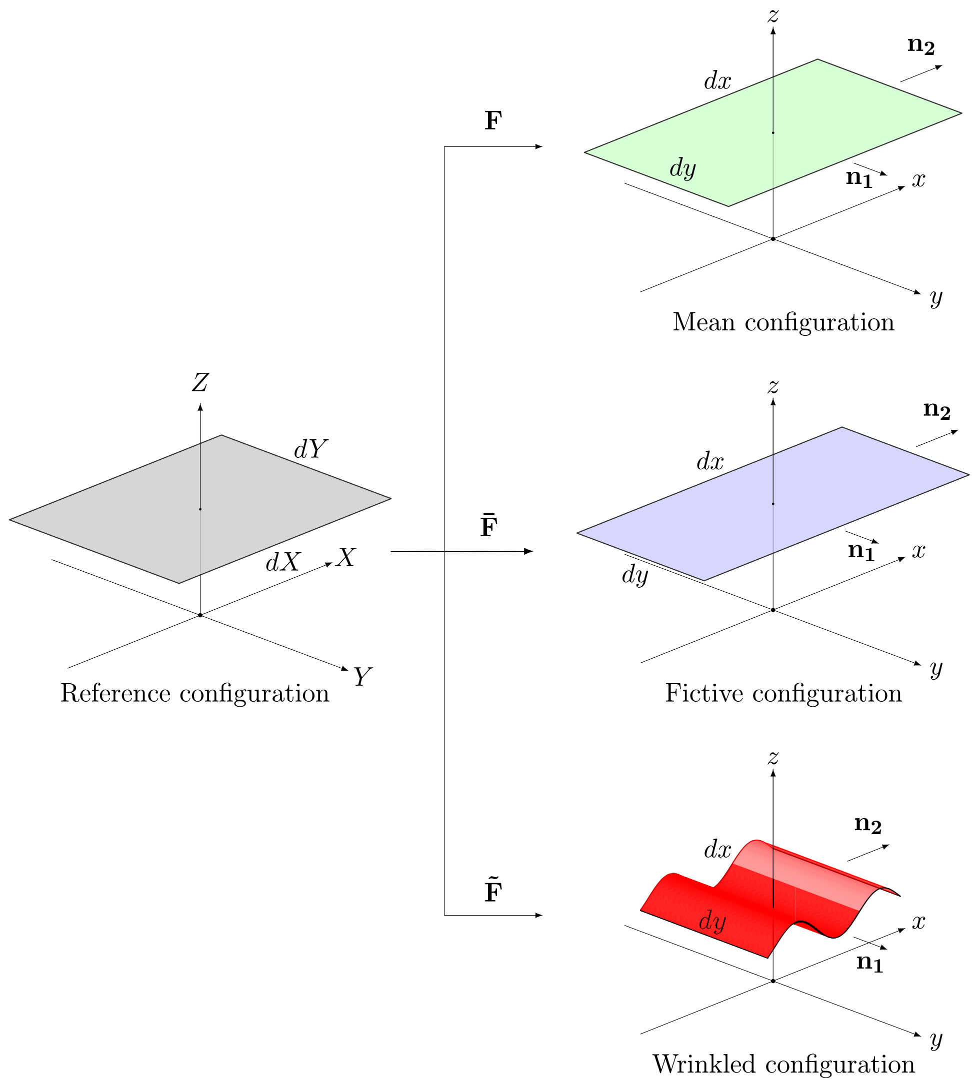

Because the mean configuration F is described by basis functions in the finite element formulation, β and $\mathbf{n_2}$ are two unknowns. As material properties and membrane theory are constructed in the reference configuration, Eq. 1 and Eq. 2 should be transformed to the reference configuration. The fictive Green-Lagrange strain tensor follows

$$\begin{aligned}\bar{\mathrm{E}} &= \frac{1}{2}(\bar{\mathrm{F}}^T \cdot \bar{\mathrm{F}} - \mathrm{I}) \\ &= \mathrm{E} + \left(\beta + \frac{\beta^2}{2}\right)\mathrm{F}^T \cdot \mathbf{n_2} \otimes \mathbf{n_2} \cdot \mathrm{F} \\ &= \mathrm{E} + \beta^* \mathbf{N_2} \otimes \mathbf{N_2}\end{aligned} \quad (6)$$

where β^* and $\mathbf{N_2}$ are the wrinkling measurement and the wrinkling direction in the reference configuration, respectively. They are the new unknowns used to replace β and $\mathbf{n_2}$. Since the membrane surface is represented in a coordinate system having two unit vectors $\mathbf{e_1}$ and $\mathbf{e_2}$, $\mathbf{N_1}$ and $\mathbf{N_2}$ can be expressed in terms of the angle of wrinkling α.

$$\begin{aligned}\mathbf{N_1} &= \cos(\alpha)\mathbf{e_1} + \sin(\alpha)\mathbf{e_2} \\ \mathbf{N_2} &= -\sin(\alpha)\mathbf{e_1} + \cos(\alpha)\mathbf{e_2}\end{aligned} \quad (7)$$

The nonlinear equations of Eq. 2 are solved to find α and β^*. Thus, the deformation gradient and the second Piola-Kirchhoff stress tensor are corrected to obtain the stress map and the wrinkled regions. Assuming the behaviour of the membrane is symmetric with respect to two semi-axes, only a quarter of the membrane geometry is considered in the computational domain. For this reason, the symmetric boundary conditions $\mathrm{u} \cdot \mathrm{e_n} = 0$ are applied on those semi-axes. Mechanical properties for the membrane material (PET) were taken from Lu and Menary (2024) and Wilson et al. (1976). The numerical simulations were performed using COMSOL Multiphysics® 6.2. The finite element domain is approximated using first-order quadrilateral elements with the largest size of about 0.2mm. The nonlinear Newton method is selected with a relative tolerance of 0.001. The results are shown in Sec. 2.1.

The predicted maps are used to avoid clamping configurations during manufacture that further provoke wrinkling by inducing excessive stress, and to understand where any occurring wrinkles might originate and why. In addition, further designs for installing ultra-thin membranes when using ultrasonic welding as the bonding process can be derived from our results.

3.2 Design for ultrasonic welding of MBRs

As was mentioned in the introduction, the previously applied design for ultrasonic welding did not allow for satisfactory welding results, as the ultra-thin membrane showed large wrinkles after installation and in some cases even tears. However, since ultrasonic welding is a well-established way of bonding PC, a revised design for the microfluidic bioreactor was created and evaluated, which was introduced in Sec. 2.2.

In general, energy directors (EDs) are an important design part when creating weld partners for ultrasonic welding. Long continuous EDs are known to require very precise manufacturing and exact process guidance. The longer a continuous ED is, the more difficult it is to meet the necessary precision in all parameters involved. An ED that consistently achieves good welds is the pillar-and-groove joint. Instead of one long ED – and thus joint – several pillar EDs are placed along the joint contour. In the counterpart of the weld pieces, the corresponding grooves are manufactured. The pillars engage into these grooves. The concept is shown in Fig. 13. The combination of pillar and groove has two main advantages: First, the grooves act as guidance for the pillars, creating an optimal fit of the chip halves. Second, the pillar-groove pair experiences a labyrinth effect for the occurring weld flash all around, which results in a very strong and tight bond. In addition, the almost point-based ED is easier to weld controlled than a long continuous ED, which is easier subject to part warping, local overwelding, or flash-showing (Rotheiser 2009; Strohfuß 2004).

The welding of the MBRs was performed on a PS DIALOG digital control ultrasonic welding machine by Herrmann Ultraschalltechnik GmbH & Co. KG, Karlsbad, Germany, which has a working frequency of 35 kHz. The revised design that uses the pillar and groove joints instead of a long continuous ED is presented in Sec. 2.2. In this section, it is also explained how the microfluidic chambers of the MBR are sealed leak-proof in the new design.

3.3 Testing completed MBRs for leakages

After the welding process, the completed MBRs were tested for leakages. For this, a glass beaker was filled with water and the top openings of the MBR were sealed with

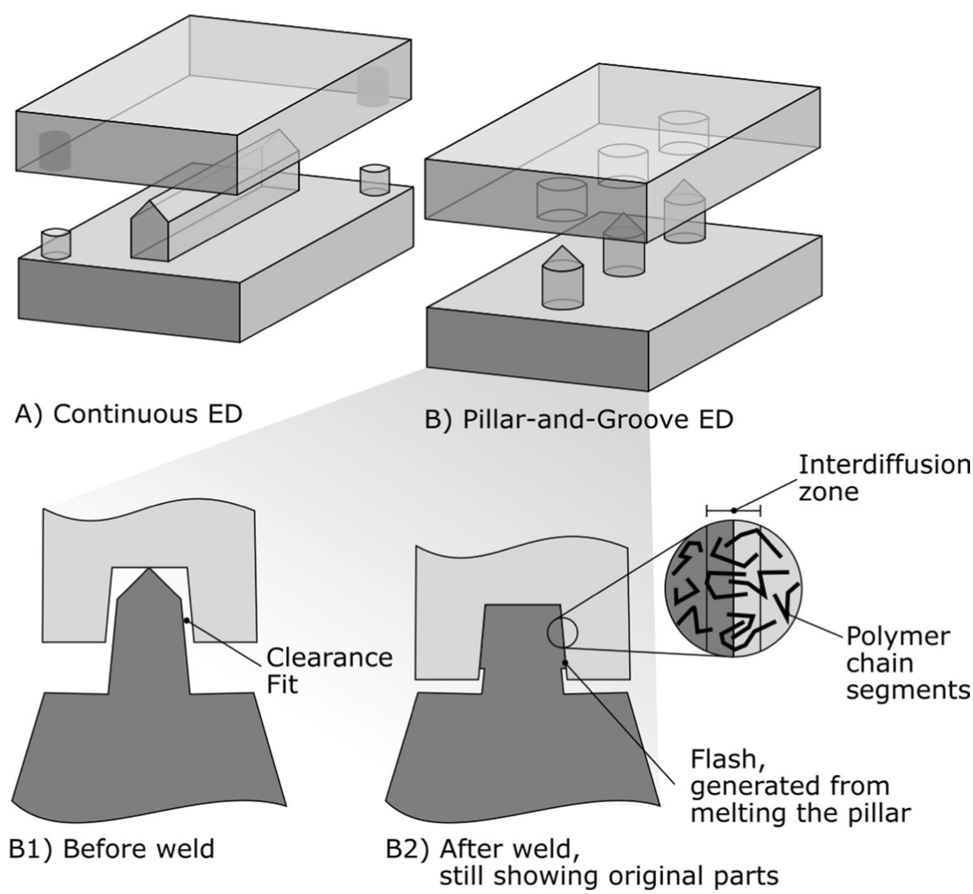

Fig. 13 Concept sketch energy directors used for ultrasonic welding. A) Sketch of a continuous ED. Additional guidance pins are necessary to achieve a precise positioning of the workpieces. **B**) Drawing of a pillar-and-groove joint-setup. For clarity, the pins are positioned very close to each other. This concept is explored in detail in 1) and 2). 1) Before the weld: Due to the material surrounding the pillar, a clear guidance during the weld is established. 2) After welding. The previous two parts have become one due to melting the pillar and part of the groove and filling this groove with the melted material (flash) from and all around the pillar. In this sketch, the two parts are still displayed with different colouration for better visibility of the process principle. In reality, a durable bond with interlocking chains, common for polymer welding, is created which ensures a strong bond. Sketches after Rotheiser (2009).

3 M™Circuit Plating Tape 851 and one of the supply channels was plugged. The second supply channel was then mounted on an outlet with compressed N_2, whose pressure was controlled. The MBR was then placed beneath the surface of the water and filled with compressed N_2 at different pressures. Figure 14 shows this setup. If leaks occurred, this approach made it easy to determine where they originated.

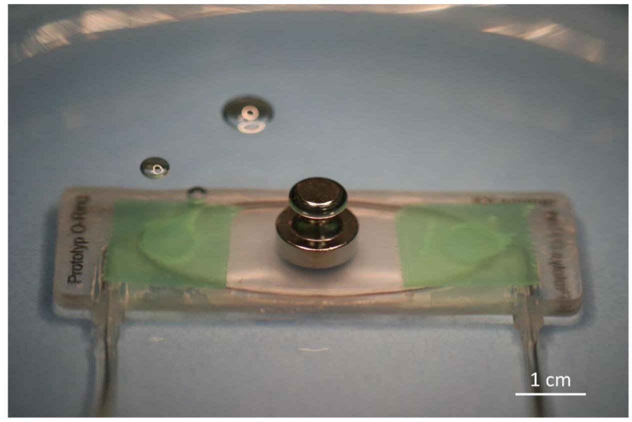

Fig. 14 Testing the MBRs for leakages at different pressures. For this, the MBR's openings in the cultivation chamber as well as one fluidic connector are sealed shut. The other fluidic connector is mounted to a controllable outlet for N_2. Next, the MBRs are placed in a glass beaker underneath the water and flooded with the N_2. If the MBR is leak-tight, the Greentape sealing the cultivation chamber will give way (like in the presented picture). If the MBR is not leak-proof, bubbles exit the MBR and, the origin of the leak becomes evident.

3.4 Validation of theoretical flow conditions

To validate the theoretical flow conditions presented in Fig. 4 finished MBRs and the resulting flow conditions were characterized as follows: Each MBR tested was filled with distilled water using a syringe pump (PHD ULTRA TM Syringe Pump Infuse/Withdraw by Harvard Apparatus, Holliston, MA, USA). When the chambers were filled and all air bubbles were removed, the openings in the cultivation chamber were sealed with transparent tape. The water supply was then swapped for a syringe with blue-dyed distilled water, which mimics the nutrient solution later applied during experiments. The blue-dyed water was then introduced into the MBR through the inlet connector at a flow rate of $20\,\mu\mathrm{L\,min}^{-1}$. The spread of this solution throughout the cultivation chamber was monitored and recorded using a monochrome camera (uEye SE (UI-2220SE-M-BG) by IDS Imaging Development Systems GmbH, Obersulm, Germany) and a Canon EOS 7D Mark II with a macro lens. This analysis was repeated with three MBRs.

4 Conclusion

The improvement achieved in the procedure for repeatable insertion of an ultra-thin membrane, as a cell migration barrier between a nutrition supply and the cell culture chamber, results in a symmetrical regularized flow profile in the chamber, ensuring that the entire chamber can be properly filled with medium. Uniform and repeatable experimental conditions could be created, which is a substantial improvement compared to the formation of major wrinkles in the previous process and the resulting uneven flow profile and nutrient distribution. The new manufacturing process consistently led to a slight but characteristic wrinkle developing along the long axis of the oval chambers. This in turn created a flow profile that had a symmetric concentration profile with an elevated central region that propagated the overall diffusion front along the axis of the chamber. However, on the edges of this spike, the flow profile was symmetric and followed the spike throughout the chamber, rapidly allowing an even distribution of nutrients throughout the chamber.

The process for installing the ultra-thin membrane in the MBR, harnessing a drumhead-stretching approach, is suitable for other application areas as well. Our design used ten pins to stretch the membrane across the oval-shaped chambers. During the ultrasonic welding process, these pins, which have corresponding holes on the other chip half, were melted, then compressed, and thus simultaneously formed an interlocking bond with the other chip half. The membrane was stretched fairly isotropically over a sealing ring which was placed between the upper and lower chip half. This sealing ring created a leak-proof seal and harmonized the uneven stress profile created when spanning the membrane across the ten pins. Overall, this design could be useful in other applications as well, for cases when a wrinkle-free installation of an ultra-thin membrane is necessary, e.g., in the field of battery cell development, medical packaging, sensor technology, catalyst development, gas contact devices, etc.

Laser transmission welding was considered as bonding method for the system as well. However, it proved to be unsuitable due to repetitive burning along the weld contour and thus, inconsistent bonding. Further information on this approach and the conducted tests can be found in the appendix.

In conclusion, the conditions for even nutrient distribution have improved to the point that repeatable plant cell cultivation experiments can now be conducted, while manufacturable, autoclavable MBRs, yielding a homogeneous flow profile, are now possible.

5 Supplementary information

The data for this article, including the data from the simulations and compression force analysis conducted for this publication, are available at KITopen at https://doi.org/10.35097/stzqf3sefnjdbt3h.

Appendix A Laser transmission welding of MBR

Laser transmission welding is a polymer bonding process frequently applied in research and development due to its flexibility in contour design and setup and comparatively easy joint design. For this research it was considered and tested as an alternative bonding method do ultrasonic welding. However, ultimately it was not suited for this use-case where an ultra-thin membrane needed to be installed between to bulk chip parts. Tests and limitations that led to this conclusion are presented in the following.

Figure 15 depicts several of the attempts to weld the MBR using laser transmission welding. The area left and right of the oval chambers where the inlet- and outlet channels connected to the chambers burnt numerous times. A reason might be that in this area, the introduced laser energy led to accumulated heat due to the dense contour in this area. However, this is not the only area where burning appeared, nor did this region burn every time. Since PC is a material that quickly yellows, and, in the next stage, easily chars, a short concentrated burn can lead to further charring down the contour path.

Furthermore, many burns seemed to originate in areas where membrane material was placed in between the two chip halves. Air pockets between welding partners are a source of burning in laser transmission welding. Thus, it is most likely that the membrane in between the chip halves may prevent a tight fit between the welding partners. This can create a larger air pocket, which then might incinerate. In addition, milling grooves from

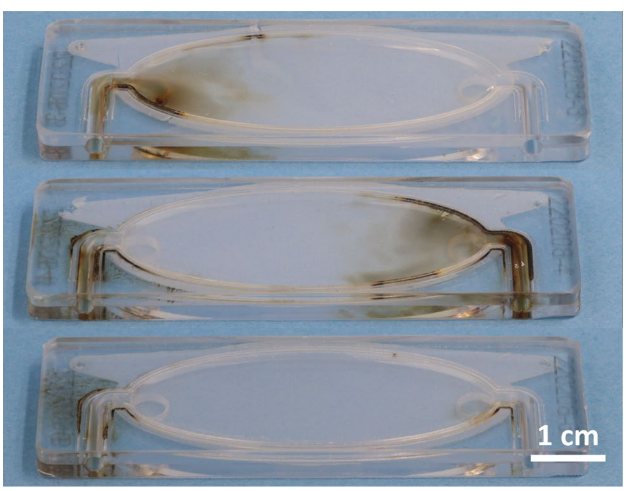

Fig. 15 Exemplary outcomes of MBR assembly using laser transmission welding. Identical laser parameters were applied. Various burns occurred during the welds at different locations. The region around the channel corners was burnt in several laser beam passes, however, it was not the only position where burns occurred, nor did these regions get burnt every time a burn developed.

manufacturing the prototypes are a possible source for creating such air pockets. For these reasons, laser welding was not pursued further as the way of welding the chip halves of the MBR together.

In general, laser transmission welding is a welding process frequently used in research and development for bonding polymers together due to its flexible contour path design as well as the locally focused energy and thus low heat deposition in the overall part. In recent years, laser welding has become a more applicable option for bonding two transparent polymer parts without the use of additives or absorbers because the newer fiber-lasers are able to emit light in the necessary wavelengths (Klein 2012; Nguyen et al. 2020). Thus, the process was applied to bond the hot embossed chip halves together. We used the laser welding system EVO 1800 produced by Evosys Laser GmbH, Erlangen, Germany. This system applies a thulium fibre laser with a wavelength of $\lambda = 1940\,\mathrm{nm}$ and can reach a maximum output power of $120\,\mathrm{W}$. The laser beam is focused using an f-theta lens which has a focal length of $437\,\mathrm{mm}$.

The chip halves and the membrane were placed in an aluminum fixture. The metal allows for a quick heat dissipation away from the part and, thus, the weld seam due to its high heat conductivity. The focal plane was adjusted to $59\,\mathrm{mm}$ underneath the contact plane of the chip halves and the membrane, to avoid burning, similar to as was done in Mamuschkin et al. (2016). To achieve a line energy E of $3\,\mathrm{J\,mm^{-1}}$ according to the formula by Nguyen et al. (2020) $E = Pn/v$, a weld power of $P = 24\,\mathrm{W}$ at a feed rate $v = 40\,\mathrm{mm\,s^{-1}}$ was chosen, with which the contour was run $n = 5$ times.

The joint has to be properly designed for a successful weld. In a best-case scenario, the laser is positioned directly above the to-be-welded area, as this creates an even heat introduction Klein (2012); Nguyen et al. (2020). Furthermore, geometrical tolerances should be kept to a minimum and the surface roughness should be as fine as possible so that the chip halves can be pressed together flush (Mamuschkin et al. 2016; Klein 2012; Nguyen et al. 2020). This is especially true when welding PC, as the material yellows easily under heat influences. If oxygen is present in a sufficient amount, this material is then likely to char and incinerate (Mamuschkin et al. 2016; Bates et al. 2015).

Appendix B Sealing-ring compression force analysis

In order to prepare the ultrasonic welding process thoroughly, the compression force of the FKM sealing rings was analyzed. This allowed for a better understanding of how much welding force is needed for a tight fit. For this, four sealing rings were analyzed, and the average was determined (Figure 16).

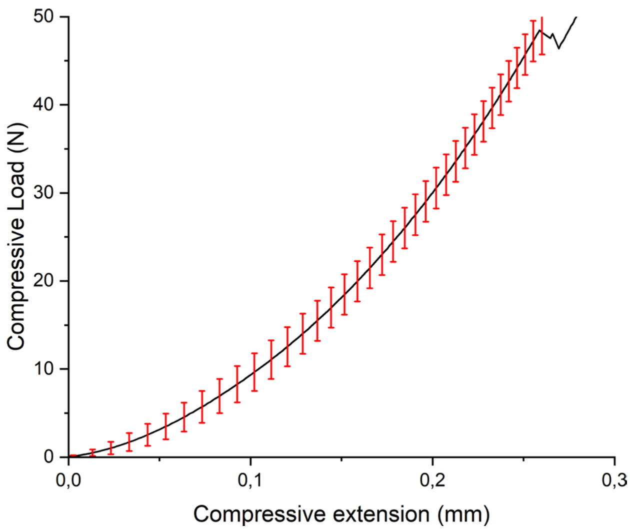

Fig. 16 Compression diagram of the FKM sealing rings. Four sealing rings were analyzed, then the average was found.

Acknowledgements This work was partly funded by the European Fund for Regional Development (INTERREG V Upper Rhine program, DialogProTec project). This work was partly carried out with the support of the Karlsruhe Nano Micro Facility (KNMF, www.knmf.kit.edu), an Open Access Research Infrastructure within the Karlsruhe High Technology Hub at the Karlsruhe Institute of Technology (KIT – The University in the Helmholtz Association, http://www.knmf.kit.edu). Furthermore, the authors thank Christian Metzger from Joseph Gottlieb Kölreuter Institute for Plant Sciences (JKIP), KIT, for conducting BY2 plant cell experiments in the MBR, Richard Thelen from IMT for support with the characterization of the MBR chip halves, Marc Schneider from IMT for hot embossing MBR chip halves, and Alexandra Moritz, André Wolfschläger and their team at the IMT for micro-milling the MBR chip halves.

Author contributions L. M. S.: Conceptualisation, methodology, validation, investigation, data curation, writing: original draft, writing: review & editing, project administration. K. C.-N.: Methodology, software, data curation, writing: original draft. L. S.: Methodology, software, validation, data curation. R. A.: Conceptualisation, writing: review & editing, supervision, project administration, funding acquisition. A. E. G.: Supervision, funding acquisition. J. G. K.: Conceptualisation, writing: review & editing, supervision, project administration, funding acquisition. D. M.: Conceptualisation, writing: review & editing, supervision, project administration.

Funding Open Access funding enabled and organized by Projekt DEAL.

Data availability The data for this article, including the data from the simulations and compression force analysis conducted for this publication, are available at KITopen at https://doi.org/10.35097/stzqf3sefnjdbt3h.

Declarations

Conflict of interest The authors have no Conflict of interest to declare that are relevant to the content of this article.

References

Okoro GO, Onu OB, Ngasoh FG, Namessan N (2019) The effect of climate change on abiotic plant stress: a review. In: Bosco de Oliveira, A. (ed.) Abiotic and biotic stress in plants. IntechOpen. Chap. 5. https://doi.org/10.5772/intechopen.77845 . https://www.intechopen.com/books/abiotic-and-biotic-stress-in-plants/the-effect-of-climate-change-on-abiotic-plant-stress-a-review Accessed 25-03-2021

Elad Y, Pertot I (2014) Climate change impacts on plant pathogens and plant diseases. J Crop Improv 28(1):99–139. https://doi.org/10.1080/15427528.2014.865412

Metzger C (2023) Ecosystem on a chip: Understanding communication between plant and fungus. PhD thesis, Karlsruher Institut für Technologie (KIT), Karlsruhe . https://doi.org/10.5445/IR/1000161004

Khattab IMA (2021) Ancestral grapes with resistance against dieback: Molecular and functional analysis of plant-pathogen crosstalk in the context of botryosphaeriaceae related dieback. Dissertation, Karlsruher Institut für Technologie (KIT), Karlsruhe . https://doi.org/10.5445/IR/1000128104

Kreppenhofer K (2013) Modular biomicrofluidics: Mikrofluidikchips im Baukastensystem für Anwendungen aus der Zellbiologie. Dissertation, Karlsruher Institut für Technologie, Karlsruhe. https://doi.org/10.5445/KSP/1000035104

Finkbeiner T (2019) Entwicklung eines mikrofluidischen Bioreaktors für die Kultivierung von Pflanzenzellen. PhD thesis, Karlsruher Institut für Technologie (KIT), Karlsruhe . https://doi.org/10.5445/IR/1000096929

Schmidt-Speicher LM, Supp L, Metzger C, Ahrens R, Nick P, Guber AE (2021) Development of a modular microfluidic bioreactor to further research the inter-cellular communication of plant cells and pathogens. In: MikroSystemTechnik Kongress 2021, pp. 543–547. VDE Verlag,

Ko J-M, Ju J, Lee S, Cha H-C (2006) Tobacco protoplast culture in a polydimethylsiloxane-based microfluidic channel. Protoplasma 227(2–4):237–240. https://doi.org/10.1007/s00709-005-0142-2

Meier M, Lucchetta EM, Ismagilov RF (2010) Chemical stimulation of the arabidopsis thaliana root using multi-laminar flow on a microfluidic chip. Lab Chip 10(16):2147–2153. https://doi.org/10.1039/c004629a. (**Accessed 2024-09-16**)

Grossmann G, Guo W-J, Ehrhardt DW, Frommer WB, Sit RV, Quake SR, Meier M (2011) The rootchip: an integrated microfluidic chip for plant science. Plant Cell 12:4234–4240. https://doi.org/10.1105/tpc.111.092577

Inc., T.F.S (2024) Polycarbonate (PC) Labware . https://www.thermofisher.com/de/de/home/life-science/lab-plasticware-supplies/plastic-material-selection/polycarbonate-pc-labware.html Accessed 2024-10-25

AdvanTech Plastics, LLC (2021) Polycarbonate: the'Clear' choice for medical devices . https://advantechplastics.com/blog/polycarbonate-the-clear-choice-for-medical-devices/ Accessed 2024-10-25

Finkbeiner T, Manz C, Raorane ML, Metzger C, Schmidt-Speicher L, Shen N, Ahrens R, Maisch J, Nick P, Guber AE (2021) A modular microfluidic bioreactor to investigate plant cell-cell interactions. Protoplasma 259(1):173–186. https://doi.org/10.1007/s00709-021-01650-0. (**Accessed 2024-08-14**)

Espinoza Orías AA, Renaud JE (2004) An optimization study of the ultrasonic welding of thin film polymers. In: Volume 1: 30th design automation conference, pp. 75–84. ASMEDC. https://doi.org/10.1115/DETC2004-57082

Tsiangou E, Teixeira de Freitas S, Villegas IF, Benedictus R (2020) Ultrasonic welding of epoxy- to polyetheretherketone- based composites: investigation on the material of the energy director and the thickness of the coupling layer. Journal of Composite Materials 54(22):3081–3098 https://doi.org/10.1177/0021998320910207

Dobrota D, Lazar SV (2021) Ultrasonic welding of pbt-gf30 (70% polybutylene terephthalate + 30 %fiber glass) and expanded polytetrafluoroethylene (e-ptfe). Polymers 13(2). https://doi.org/10.3390/polym13020298

Korycki A, Carassus F, Garnier C, Chabert F, Djilali T (2023) Effect of energy director thickness on thermal diffusion and joint quality during ultrasonic welding of cf/peek composites. In: Madej, L., Sitko, M., Perzynski, K. (eds.) Material Forming 26th International ESAFORM Conference on Material Forming (ESAFORM 2023). Materials Research Proceedings, vol. 28, pp. 1819–1828. Materials Research Forum LLC, Millersville, PA, USA . https://doi.org/10.21741/9781644902479-197 . Accessed 2024-01-08

Brosda M, Nguyen P, Olowinsky A, Gillner A (2020) Analysis of the interaction process during lasertransmission welding of multilayer polymer films with adapted laser wavelength by numerical simulation and thermography. J Laser Appl 32(2):23. https://doi.org/10.2351/7.0000113

Shah R (2012) To seam or not to seam: polyzen creates a robust seam in RF welding of ultra-thin films . https://www.polyzen.com/2012/04/25/seam-not-seam-polyzen-creates-robust-seam-rf-welding-ultra-thin-films/ Accessed 2024-01-08

Tang N, Li Y, Ge J, Si Y, Yu J, Yin X, Ding B (2020) Ultrathin cellulose voronoi-nanonet membranes enable high-flux and energy-saving water purification. ACS Appl Mater Interfaces 12(28):31852–31862. https://doi.org/10.1021/acsami.0c08504

Li Q, Mu Z, Luo M, Huang A, Pang S (2021) Laser spot micro-welding of ultra-thin steel sheet. Micromachines 12(3):342. https://doi.org/10.3390/mi12030342

Focke M, Kosse D, Müller C, Reinecke H, Zengerle R, Stetten F (2010) Lab-on-a-foil: microfluidics on thin and flexible films. Lab Chip 10(11):1365–1386. https://doi.org/10.1039/c001195a

Jong J, Lammertink RGH, Wessling M (2006) Membranes and microfluidics: a review. Lab Chip 6(9):1125–1139. https://doi.org/10.1039/B603275C

Boeltken T, Wunsch A, Gietzelt T, Pfeifer P, Dittmeyer R (2014) Ultracompact microstructured methane steam reformer with integrated palladium membrane for on-site production of pure hydrogen: Experimental demonstration. Int J Hydrogen Energy 41:18058–18068. https://doi.org/10.5445/IR/110100686

Dang QK, Chang P-L, Dang TN, Weng F, Uan J-Y, Wang D-A (2019) Ultrasonic spot welds of gas diffusion layer to proton exchange membrane of fuel cells. J Mater Process Technol 266(266):208–216. https://doi.org/10.1016/j.jmatprotec.2018.11.004

Qiu J, Zhang G, Sakai E, Liu W, Zang L (2020) Thermal welding by the third phase between polymers: a review for ultrasonic weld technology developments. Polymers 12(4):759. https://doi.org/10.3390/polym12040759

Iwasiro S, Watanabe A, Onozuka Y, Minai M, Nishimura H, Takeuchi S (2014) Development and estimation of brain tumor cells culture flask with acoustic window film for ultrasound exposure. Japanese J Appl Phys 53(7S) https://doi.org/10.7567/JJAP.53.07KF12

Scheffler TB, Leao AJ (2008) Fabrication of polymer film heat transfer elements for energy efficient multi-effect distillation. Desalination 222(1–3):696–710. https://doi.org/10.1016/j.desal.2007.02.076

Wood E, Blasko M(2024) Technology Comparison: Laser Welding vs. Hot-plate Welding in Automotive Lighting. https://www.machinedesign.com/fastening-joining/article/55041926/emerson-technology-comparison-laser-welding-vs-hot-plate-welding-in-automotive-lighting Accessed 2024-06-11

Plastic Welding Solutions M (2024) Welding technologies. https://www.mecasonic.com/en/technologies/ Accessed 2024-06-11

Potente H (2004) Fügen Von Kunststoffen: Grundlagen, Verfahren, Anwendung; Mit 31 Tabellen. Hanser, München and Wien

Rotheiser J (2009) Joining of plastics: handbook for designers and engineers, 3rd edn. Hanser, Cincinnati, Ohio and Munich . https://doi.org/10.3139/9781569904961

Dahlstrand D (2017) How to solve common ultrasonic welding problems: understand and address the likely origins of welding problems to keep production on track., Cincinnati, Ohio, USA . https://www.ptonline.com/articles/how-to-solve-common-ultrasonic-welding-problems Accessed 2024-01-17

Speicher LM, Metzger C, Ahrens R, Mager D, Guber AE, Korvink JG (2023) Wrinkle-free bonding of thin membranes in a microfluidic bioreactor. In: MikroSystemTechnik Kongress 2023, pp. 233–236. VDE Verlag,

Dukane intelligent assembly solutions: guide to ultrasonic plastics assembly, St. Charles, IL, USA. https://documents.dukane.com/DesignGuides/Guide%20To%20US%20Plastic%20Assembly.pdf Accessed 2024-01-17

Beck WA, Huang M, Ketterl J, Hughes T (2002) IR laser welding of thin polymer films as a fabrication method for polymer mems. In: Zimnyakov, D.A., Derbov, V.L., Melnikov, L.A., Babkov, L.M. (eds.) Saratov Fall Meeting 2002: laser physics and photonics, spectroscopy, and molecular modeling III; coherent optics of ordered and random media III. SPIE Proceedings, vol. 1, pp. 167–178. SPIE, Bellingham, WA, USA . https://doi.org/10.1117/12.518600

Brosda M, Nguyen NP, Olowinksy A, Gillner A (2020) Investigations on the influence of beam shaping in lasertransmission welding of multi-layer polymer films with wavelength-adapted diode laser beam sources. In: Da Silva, L.F.M., Martins, P.A.F., El-Zein, M.S. (eds.) Advanced Joining Processes. Springer eBook Collection, pp. 91–100. Springer Singapore and Imprint Springer, Singapore . https://doi.org/10.1007/978-981-15-2957-3_7

Pagano N, Campana G, Fiorini M, Morelli R (2017) Laser transmission welding of polylactide to aluminium thin films for applications in the food-packaging industry. Optics Laser Technol 91:80–84. https://doi.org/10.1016/j.optlastec.2016.12.014

Klotzbuecher T, Letschert M, Braune T, Drese KS, Doll T (2006) Diode laser welding for packaging of transparent micro-structured polymer chips. In: Bachmann, F.G., Hoving, W., Lu, Y., Washio, K. (eds.) Laser-based Micropackaging. SPIE Proceedings. SPIE, https://doi.org/10.1117/12.649248

Jiang X, Chandrasekar S, Wang C (2015) A laser microwelding method for assembly of polymer based microfluidic devices. Opt Lasers Eng 66:98–104. https://doi.org/10.1016/j.optlaseng.2014.08.014

Liu H, Jiang Y, Tan W, Chen G, Liu W, Wang X (2017) The study of laser transmission joining PA66 and PVC with large compatibility difference. J Manuf Process 26:252–261. https://doi.org/10.1016/j.jmapro.2017.02.024

Brown N, Kerr D, Jackson MR, Parkin RM (2000) Laser welding of thin polymer films to container substrates for aseptic packaging. Optics Laser Technol 32(2):139–146. https://doi.org/10.1016/S0030-3992(00)00033-5. (**Accessed 2024-01-12**)

Roddeman DG, Drukker J, Oomens CWJ, Janssen JD (1987) The wrinkling of thin membranes: part I-theory. J Appl Mech Trans ASME 54:884–887. https://doi.org/10.1115/1.3173133

Lu H, Menary G (2024) Determination of Young's modulus of PET sheets from lamb wave velocity measurement. Exp Mech 64(3):377–391. https://doi.org/10.1007/s11340-024-01039-z. (**Accessed 2026-02-14**)

Wilson I, Cunningham A, Ward IM (1976) The determination of Poisson's ratio compliances for polyethylene terephthalate sheets using a Michelson interferometer. J Mater Sci 11(12):2181–2188. https://doi.org/10.1007/BF00752081. (**Accessed 2026-02-14**)

Strohfuß W (2004) Ultraschallschweißen. In: Ehrenstein GW (ed) Handbuch Kunststoff-Verbindungstechnik. Carl Hanser Verlag, München, pp 257–279

Klein R (2012) Laser Welding of Plastics. Wiley-VCH, Weinheim . https://doi.org/10.1002/9783527636969 . http://site.ebrary.com/lib/alltitles/docDetail.action?docID=10716631

Nguyen N-P, Behrens S, Brosda M, Olowinsky A, Gillner A (2020) Laser transmission welding of absorber-free semi-crystalline polypropylene by using a quasi-simultaneous irradiation strategy. Welding World 64(7):1227–1235. https://doi.org/10.1007/s40194-020-00913-3

Mamuschkin V, Engelmann C, Olowinsky A (2016) Improvement of energy deposition in absorber-free laser welding through quasi-simultaneous irradiation. Phys Procedia 83:472–482. https://doi.org/10.1016/j.phpro.2016.08.049

Bates PJ, Okoro TB, Chen M (2015) Thermal degradation of PC and PA6 during lasertransmission welding. Welding World 59(3):381–390. https://doi.org/10.1007/s40194-014-0209-9